

In vivo oral imaging with integrated portable photoacoustic microscopy and optical coherence tomography

Wei Qin, Weizhi Qi, Tian Jin, Heng Guo, and Lei Xi

Citation: *Appl. Phys. Lett.* **111**, 263704 (2017);

View online: <https://doi.org/10.1063/1.5006234>

View Table of Contents: <http://aip.scitation.org/toc/apl/111/26>

Published by the [American Institute of Physics](#)

A banner for SciLight featuring a dark blue background with a network of glowing yellow and blue nodes connected by thin lines. The text is positioned on the left side of the banner.

SciLight

Sharp, quick summaries **illuminating**
the latest physics research

Sign up for **FREE!**

AIP
Publishing

In vivo oral imaging with integrated portable photoacoustic microscopy and optical coherence tomography

Wei Qin,^{1,a)} Weizhi Qi,^{1,a)} Tian Jin,¹ Heng Guo,¹ and Lei Xi^{1,2,b)}

¹School of Physical Electronics, University of Electronic Science and Technology of China, Chengdu 610054, China

²Center for Information in Medicine, University of Electronic Science and Technology of China, Chengdu 610054, China

(Received 23 September 2017; accepted 13 December 2017; published online 28 December 2017)

Oral diseases, especially oral cancers, are becoming serious health problems in humans. To image vasculatures and structures simultaneously in the human oral cavity which are tightly associated with various oral diseases, we develop a dual-modality portable optical resolution photoacoustic microscopy (ORPAM) and optical coherence tomography (OCT) system. This system utilizes a new rotary scanning mechanism and a compact design of the imaging head, making it portable and free of translation of the imaging interface or samples. Through the phantom experiments, both modalities yield high lateral resolutions of 8.1 μm (ORPAM) and 8.56 μm (OCT), respectively. The axial resolutions are measured to be 116.5 μm for ORPAM and 6.1 μm for OCT. *In vivo* imaging of a mouse ear was carried out to evaluate the performance of the system in biological tissues. In addition, *in vivo* oral imaging of a healthy human lip and monitoring recovery progress of a lip ulcer demonstrate the clinical potential of this system. *Published by AIP Publishing.*

<https://doi.org/10.1063/1.5006234>

Cancer is a major public health problem around the world. In the United States, there were 1 688 780 new cases and 600 920 deaths in 2017, of which 49 670 new cases and 9700 deaths are associated with oral cancers.¹ Fortunately, early diagnosis and treatment can substantially improve the survival rate and life quality of cancer patients. Recent studies show that angiogenesis and minor structural abnormality are tightly related to the early cancerization of oral tumor lesions. To date, various different optical imaging methods have been applied to oral imaging such as confocal microscopy,² multi-spectral optical imaging,³ multiphoton microscopy,⁴ and optical coherence tomography (OCT).⁵

OCT was first proposed in 1991 by Huang *et al.* and further promoted to spectral domain optical coherence tomography (SD-OCT) and swept source optical coherence tomography (SS-OCT).^{6,7} OCT is capable of visualizing microstructures of biological tissues with a high spatiotemporal resolution and a deep penetration depth. Recently, OCT angiography (OCTA), in which the imaging contrast comes from blood flow, allows high-resolution visualization of microvasculature and has been successfully demonstrated in human oral imaging.^{8,9} However, it still suffers from multiple scans and difficulties in deriving absorption associated parameters such as concentrations of oxyhemoglobin and deoxyhemoglobin and oxygen saturation. Photoacoustic imaging is a noninvasive imaging technique based on the absorption of light.^{10,11} Optical resolution photoacoustic microscopy (ORPAM) is one of the photoacoustic microscopies that enable high spatiotemporal resolution and deep penetration depth without axial scanning.¹² Compared with OCTA, ORPAM is free of speckle noise and can

quantitatively derive functional parameters using the multi-spectral strategy.^{12,13} However, ORPAM lacks sufficient sensitivity to visualize structures of low light-absorbing organs/tissues. Therefore, a hybrid imaging system combining OCT with ORPAM can visualize both the microstructure and the microvasculature of biological tissues. Several dual-modality ORPAM-OCT systems have been proposed for different applications. Li *et al.* utilized a hybrid scanning mechanism, integrating a cylindrically focused transducer coupled with a one dimensional galvanometer scanner (GVS) and a linear motorized stage, to achieve dual-modality ORPAM and OCT imaging.¹⁴ Zhang *et al.* reported an integrated photoacoustic imaging and OCT system based on all optical detection for human palm imaging.¹⁵ Xi *et al.* developed an endoscopic probe combining ORPAM with OCT using a GRIN lens.¹⁶ Zhang *et al.* proposed the use of a single visible light source for both ORPAM and OCT imaging.¹⁷ Liu *et al.* show a multi-modality system integrating photoacoustic tomography, optical coherence tomography, and OCT angiography systems for *in vivo* human skin imaging.¹⁸ Unfortunately, most of the reported ORPAM-OCT systems are inaccessible to the human oral cavity due to one or several of the following limitations: low temporal resolution, bulky size, small field of view (FOV), and inconvenience of the equipment. In this study, we develop a dual-modality rotary scanning based ORPAM and OCT system for oral inspection of humans. The rotary-based scanning mechanism and compact design enable translationless of imaging interface/samples and make it portable for clinical use. Besides phantom evaluation and animal experiments, we demonstrate an *in vivo* study of a lip ulcer in a volunteer's oral cavity using this portable system and carry out quantitative analysis including standard deviation of OCT A-lines, concertation of total hemoglobin, and size of the ulcer wounds for further clinical diagnosis of oral diseases.¹⁹

^{a)}W. Qin and W. Qi contributed equally to this work.

^{b)}Author to whom correspondence should be addressed: xilei1985@uestc.edu.cn

Figure 1 shows the layout of the system and the volumetric rendering of the imaging probe. In ORPAM, 532 nm laser pulses with a duration of 7 ns emanating from a high-repetition-rate (20 kHz) laser (FQS-200-1-Y-532, Elforlight) are coupled to a single mode fiber by an objective (O1), collimated using a fiber collimator (F220FC-532, Thorlabs Inc.), reflected by a dichroic mirror (DMLP650, Thorlabs Inc.), and delivered into a two-dimensional (2D) galvanometer scanner (GVS002/M, Thorlabs Inc.). The scanner is driven using a multifunctional data acquisition card (PCI-6731, National Instrument) and moves the laser beam on the back of a scan lens (SL) (LSM03-BB, Thorlabs Inc.). The focused light beam passes through a cover glass (CG), a water cube, and a sealing membrane (SM) to illuminate the sample. The induced photoacoustic (PA) signals, reflected by the tilted cover glass in the water cube, are captured by a 15 MHz cylindrically focused transducer (V324, Olympus) which is mounted on a motorized rotator (RSA100, Zolix) and has a focal length of 38 mm, a center frequency of 15 MHz, an active area of 6 mm, and a bandwidth of 75%. The PA signals are amplified by an ~ 28 dB pre-amplifier (ZFL-500LN, Mini Circuits) and an ~ 39 dB amplifier (5073PR, Olympus) and digitized using a high-resolution data acquisition card (PCI-5122, National Instruments) at a sampling rate of 100 MS/s.

The OCT unit employs a superluminescent diode (SLD-371, SUPERLUM) with a center wavelength of 839.8 nm and a full width at half maximum (FWHM) bandwidth of 51.8 nm. After passing through an isolator, the light is coupled to a 2×2 fiber coupler (TW850R5A2, Thorlabs Inc.). Light beams in both reference and sample arms are collimated using a collimator (F260APC-780, Thorlabs) and an aspheric lens (AL), respectively. As shown in Fig. 1(b), the aspheric lens is fixed on a translation stage and adjusted to make the optical focus of OCT confocal with the optical focus of ORPAM. Two fiber-based polarization controllers (FPC023, Thorlabs) are used to adjust the light polarization in both reference and sample arms. The sample beam passes through the dichroic mirror to merge with the ORPAM light path. The reference beam is focused by an objective and reflected by a mirror. The interfered light signals are detected by a homemade spectrometer consisting of a collimator (F810APC-780, Thorlabs), a 1200-line grating, a doublet lens (GCL-010604, Daheng Optics), a line scan CCD

(spl2048-140 km, Basler), and a high-speed frame grabber board (PCIe-1427, National Instruments).

The rotary-based scanning mechanism has been described in detail in our previous publications.^{20–22} We carried out *in vivo* ORPAM and OCT experiments simultaneously by acquiring 1000 A-lines with a step interval of $6 \mu\text{m}$ and 1000 B-scans with an angular interval of 1.8° . Considering that the maximal repetition rate of the laser is up to 20 kHz, each experiment costs 55 s. In phantom experiments to evaluate the spatial resolutions of both ORPAM and OCT, we collected 2000 A-lines with a $3 \mu\text{m}$ interval to form a B-scan and 3600 B-scans with a 0.05° rotational angle to reconstruct a volumetric image.

To evaluate the spatial resolutions and signal to noise ratios (SNRs) of both imaging modalities, we imaged a sharp blade edge and carbon fibers, respectively, which are embedded in a tissue mimicking phantom with a given optical absorption coefficient of 0.01 mm^{-1} and a reduced scattering coefficient of 1.0 mm^{-1} by mixing agarose, intralipid, and India ink.

Mice were freely laid down on a heating pad to maintain the body temperature at 37°C and anaesthetized with chloral hydrate (50 mg/kg) by intraperitoneal injection. The mouse ears were gently depilated to remove the strong influence of hairs. All the procedures have been approved by the University of Electronic Science and Technology of China (UESTC).

We imaged the lips of a male volunteer with a self-developed ulcer in the lip. During the experiments, the volunteer wore a protection glass to avoid the potential damage of laser beams to the eyes. He sat on a chair and the image head was adjusted in order to align the imaging window with the selected region of his lower lip. After the experiments, dentists continued to examine the imaged area for 7 days and no abnormal symptom was observed. [Supplementary material S2](#) shows a photograph of the volunteer participating in oral imaging. We have obtained consent from the volunteer participating in the experiments.

We calculated total hemoglobin (HbT) and the area of the wound based on ORPAM data. In photoacoustic imaging using the wavelength of 532 nm, the intensity of the photoacoustic signal is positively proportional to the concentration of total hemoglobin. To derive the relative concentration of HbT, we summed all the photoacoustic signals over the

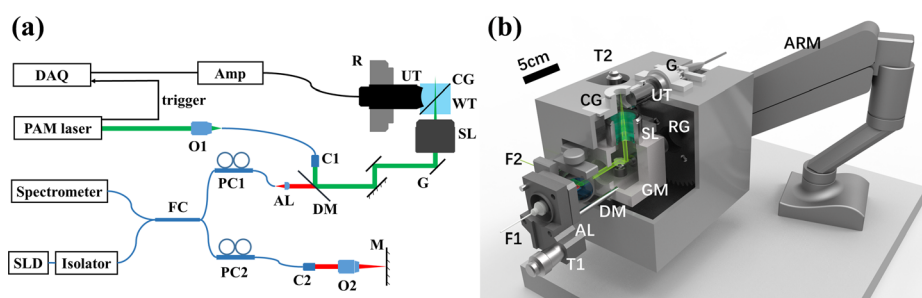


FIG. 1. The schematic of the integrated ORPAM-OCT system and the volumetric rendering of the imaging probe. (a) The layout of the system. (b) 3-D rendering of the imaging probe with a size of $170 \text{ mm} \times 135 \text{ mm} \times 140 \text{ mm}$. Scale bar: 5 cm. O1–O2, objective lens; C1–C2, collimator; FC, fiber coupler; PC1–PC2, fiber polarization controller; M, mirror; AL, aspheric lens; DM, dichroic mirror; G, galvanometer; SL, scan lens; WT, water tank; CG, cover glass; UT, ultrasound transducer; R, rotator. F1–F2, optical fibers; T1–T2, translation stage; RG, rotator and gear; G, gear. [Supplementary material S1](#) shows a photograph of the dual-modality system.

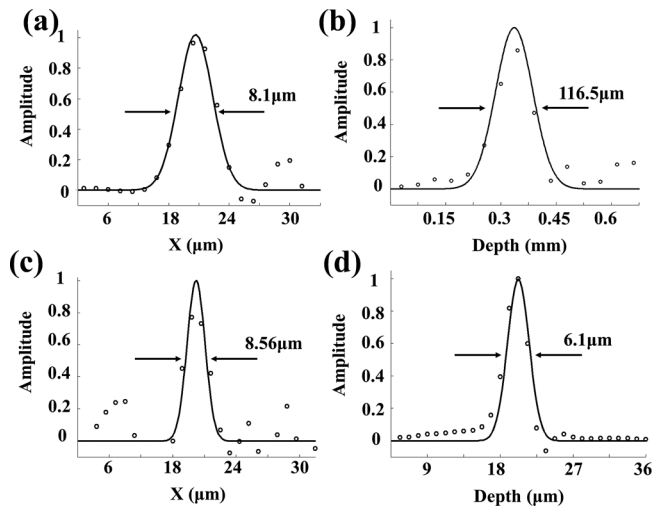


FIG. 2. Spatial resolutions of the system. (a) The fitted line spread function (LSF) of the blade edge (ORPAM). (b) The fitted point spread function (PSF) of a Hilbert transformed A-line (ORPAM). (c) The fitted line spread function (LSF) of the imaged edge (OCT). (d) The fitted point spread function (PSF) of a mirror surface (OCT).

entire imaging area and normalized the values derived from stages of the ulcer. The area of the wound was calculated and normalized with the assumption that the geometry of the wound was ellipse. The standard deviation of OCT A-lines, which represented the structural changes of oral tissues and tightly associated with early cancerizations, was calculated using a reported method.¹⁹

We first characterized the performance of the system using phantom experiments. Figure 2 presents the spatial resolutions of both modalities. We derived the line spread functions (LSFs) of the blade for both ORPAM and OCT to estimate the lateral resolutions. As shown in Figs. 2(a) and 2(c), the lateral resolutions of ORPAM and OCT are calculated to be $8.1 \mu\text{m}$ and $8.56 \mu\text{m}$, respectively.

The axial resolution of OCT was evaluated using a mirror surface serving as a perfect reflector. The axial resolution of ORPAM was estimated through deriving the FWHM of the Gaussian-fitted profile of a typical Hilbert transformed A-line. As presented in Figs. 2(b) and 2(d), the axial resolutions of ORPAM and OCT are $116.5 \mu\text{m}$ and $6.1 \mu\text{m}$,

respectively. In addition, the SNRs of OCT and ORPAM are measured to be 52 dB and 40 dB with a carbon fiber phantom.

We further evaluated the performance of the system using a mouse ear and a healthy human lip. Figure 3(a) presents the ORPAM maximum amplitude projection (MAP) of the vascular network in a mouse ear. Figure 3(b) shows the OCT MAP of the same mouse ear, in which signals in the area indicated by the white arrow are saturated due to the strong reflection of the sealing plastic membrane. The OCT and ORPAM B-scans along the white dotted lines in Figs. 3(a) and 3(b) are presented in Fig. 3(c). The animal results suggest that ORPAM is able to visualize the distribution of large blood vessels, small blood vessels, and capillaries as presented in Fig. 3(a), while OCT provides the structures including epidermis, dermis, and cartilage as shown in the Fig. 3(c).

Figures 3(d) (Multimedia view) and 3(e) present the ORPAM and OCT MAPs of a healthy lower lip. Figure 3(f) shows the B-scans of ORPAM and OCT along the white dotted line in Figs. 3(d) (Multimedia view) and 3(e). The MAP image of ORPAM shows the microvascular distribution in the lip. Visualization 1 shows the slice of the ORPAM volume data of Fig. 3(d) (Multimedia view) in depth. Within the top surface of the lip tissue, there are numerous capillary loops which will bend and twist in the early stage of oral cancer.²³ In comparison, OCT provides the microstructures including epidermis and lamina propria.

To show the clinical feasibility of this probe to screen or diagnose oral diseases, we carried out longitudinal *in vivo* imaging of a human lip ulcer to monitor the healing process. In Fig. 4, the first row shows the ORPAM MAP images, and the second and third rows present the B-scans of ORPAM and OCT, respectively. We highlight the wound areas in different stages with dashed yellow circles in the first row. From day 1 to day 3, the ulcer was developing and thus the wound deteriorated. From day 4, the wound started to heal with the growth of blood vessels from the boundary to the center. In the second row, as indicated by white arrows, selected ORPAM B-scans show the healing progress of blood vessels in the wound. Apart from ORPAM, as shown in the third row, OCT B-scans show the structural changes

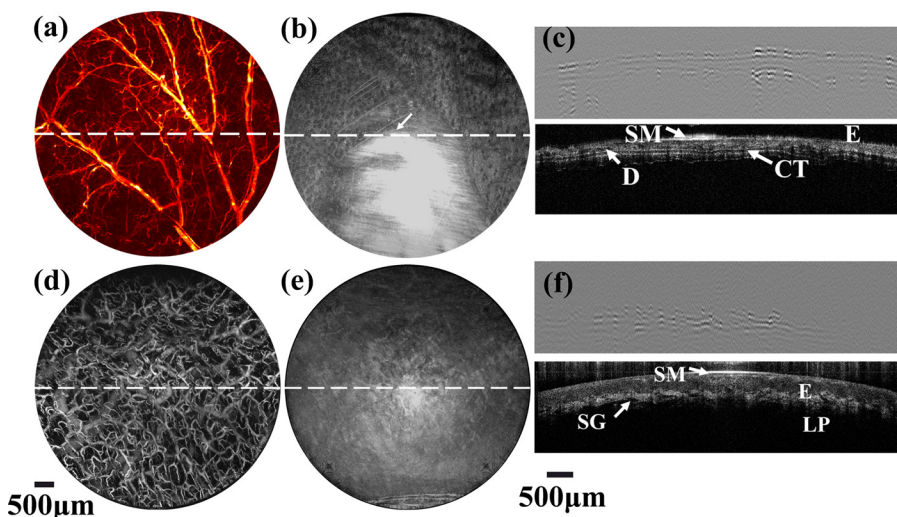


FIG. 3. Dual-modality imaging results of a mouse ear and a human lip. (a) Projected ORPAM image of a mouse ear. (b) OCT MAP image of the same mouse ear in (a). (c) Typical ORPAM and OCT B-scans along the white dotted line in (a) and (b). (d) Projected ORPAM image of a healthy human lip. (e) OCT MAP image of the same area in (d). (f) Typical ORPAM and OCT B-scans along the white dotted line in (d) and (e). SM, sealing membrane; E, epidermis; D, dermis; CT, cartilage; SG, salivary gland; LP, lamina propria. Scale bar: $500 \mu\text{m}$. Multimedia view: <https://doi.org/10.1063/1.5006234.1>

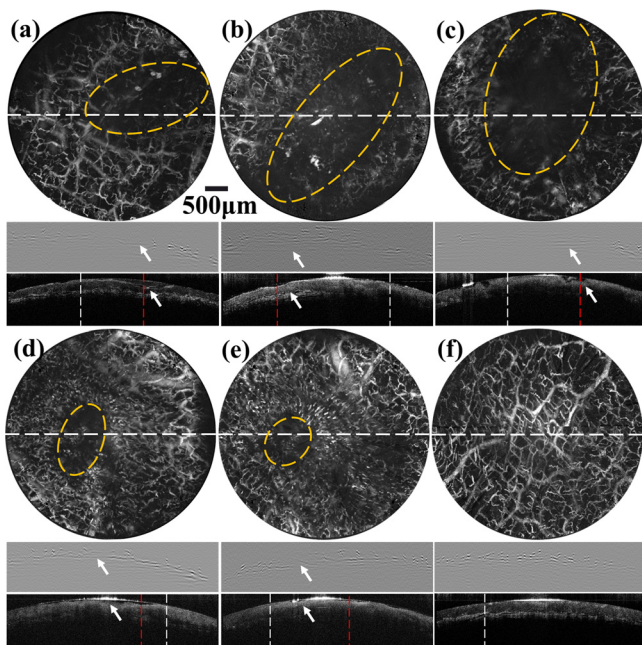


FIG. 4. ORPAM and OCT results of the microvascular distribution and microstructures of the lower lip during the healing process of an ulcer wound. Row 1 in (a) to (f), The ORPAM MAP images of the lip from day 1 to day 6. Row 2 in (a) to (f), ORPAM B-scans of the lip along the dashed white lines in Row1. Row3 in (a) to (f), OCT B-scans of the lip along the dashed white lines in Row1. The wounds are indicated by the yellow circles in ORPAM MAP images and the white arrows in ORPAM B-scans. The A-line profiles indicated by the white and yellow dashed lines in OCT B-scans are shown in [supplementary material S3](#). Scale bars: 500 μm .

during the healing progress. The white and red dashed lines indicate the positions of A-lines selected for quantitative analyses. The derived values of HbT, wound area, and standard deviations of normal and impaired tissues across the entire recovery of the ulcer are presented in Table I. At the early stage of the ulcer, the loss of blood vessels in the wound leads to the significant decrease in the total hemoglobin. When the ulcer starts to recover, the regenerated blood vessels result in the increase of the total hemoglobin. In addition, the changes of the wound area are consistent with those of total hemoglobin. Based on OCT data, we notice that the standard deviations of A-lines in both normal and impaired tissues do not change over time. However, the standard deviation (SD II) of A-lines in impaired tissues is higher than the standard deviation (SD I) of A-lines in normal tissues.¹⁹

One of the major challenges for ORPAM is the lack of an appropriate clinical application. Oral diseases such as ulcers, oral cancer, and mucosal infections are tightly associated with the changes of the microvasculature and microstructure. Unfortunately, all existing ORPAMs are not

TABLE I. Quantitative analysis based on ORPAM and OCT images.

	HbT	Area	SD I	SD II
Day 1	0.4126	0.469	0.0985	0.1277
Day 2	0.1908	0.8365	0.0854	0.1254
Day 3	0.0877	1.0	0.0881	0.1144
Day 4	0.4043	0.2835	0.0980	0.1069
Day 5	0.6843	0.1221	0.0802	0.1035
Day 6	1.0	0	0.0878	...

applicable for human oral imaging due to the inconvenience of the equipment. We propose the rotary-scanning-based ORPAM with a compact and portable configuration, making it accessible to human oral imaging. However, based on the principle of photoacoustic imaging, ORPAM has difficulties in resolving microstructures. Thus, we integrate ORPAM and OCT in this portable probe to simultaneously visualize both the microvasculature and the microstructure of oral tissues. To demonstrate the clinical feasibility, we applied this system to monitor the recovery of an ulcer wound in a volunteer's lip and carried out quantitative analyses based on ORPAM and OCT images. Before the clinical translation of this system, we still need to do further improvements. First, a functional ORPAM system with multi-wavelength illuminations and a Doppler OCT will allow derivation of functional parameters such as blood oxygenation, oxygen saturation, and blood velocity. Second, to cover the entire oral cavity, especially uneven regions, miniaturization is necessary. Finally, a laser source with a higher repetition rate can be used to accelerate the imaging speed.

See [supplementary material](#) for the photographs of the dual-modality system and the volunteer participating in the oral imaging experiment and the OCT A-lines used to carry out quantitative analysis.

This study was supported by the National Natural Science Foundation of China (61775028, 61528401, and 81571722); State International Collaboration Program from Sichuan (2016HH0019); and startup Grant (No. A03012023601011) from the University of Electronic Science and Technology of China. We thank the volunteer for participating in the experiments.

- ¹R. L. Siegel, K. D. Miller, and A. Jemal, *CA Cancer J. Clin.* **67**(1), 7 (2017).
- ²A. L. Clark, A. M. Gillenwater, T. G. Collier, R. Alizadehneri, A. K. Elnaggar, and R. Richardskourtum, *Clin. Cancer Res.* **9**(13), 4714 (2003).
- ³D. Roblyer, R. Richardskourtum, K. Sokolov, A. K. Elnaggar, M. D. Williams, C. Kurachi, and A. M. Gillenwater, *J. Biomed. Opt.* **13**(2), 024019 (2008).
- ⁴P. Wildersmith, W. Jung, M. Brenner, K. Osann, H. Beydoun, D. V. Messadi, and Z. Chen, *Lasers Surg. Med.* **35**(2), 96 (2004).
- ⁵J. M. Ridgway, W. B. Armstrong, S. Guo, U. Mahmood, J. Su, R. P. Jackson, T. Shibuya, R. L. Crumley, M. Gu, Z. Chen *et al.*, *Arch. Otolaryngol.* **132**(10), 1074 (2006).
- ⁶J. F. D. Boer, B. Cense, B. H. Park, M. C. Pierce, G. J. Tearney, and B. E. Bouma, *Opt. Lett.* **28**(21), 2067 (2003).
- ⁷R. Huber, D. C. Adler, and J. G. Fujimoto, *Opt. Lett.* **31**(20), 2975 (2006).
- ⁸Y. Jia, S. T. Bailey, T. S. Hwang, S. M. McClintic, S. S. Gao, M. E. Pennesi, C. J. Flaxel, A. K. Lauer, D. J. Wilson, J. Hornegger *et al.*, *Proc. Natl. Acad. Sci. U. S. A.* **112**(18), E2395–E2402 (2015).
- ⁹R. F. Spaide, J. M. Klancnik, and M. J. Cooney, *JAMA Ophthalmol.* **133**(1), 45 (2015).
- ¹⁰L. V. Wang and S. Hu, *Science* **335**(6075), 1458 (2012).
- ¹¹P. C. Beard, *Interface Focus* **1**(4), 602 (2011).
- ¹²S. Hu, K. Maslov, and L. V. Wang, *Opt. Lett.* **36**(7), 1134 (2011).
- ¹³S. Hu, K. Maslov, and L. V. Wang, *Med. Phys.* **36**(6), 2320 (2009).
- ¹⁴L. Li, B. Rao, K. Maslov, and L. V. Wang, *Proc. SPIE* **7564**, 75641Z-1 (2010).
- ¹⁵E. Zhang, B. Povazay, J. Laufer, A. Alex, B. Hofer, B. Pedley, C. Glittenberg, B. Treeby, B. Cox, and P. Beard, *Biomed. Opt. Express* **2**(8), 2202 (2011).
- ¹⁶L. Xi, C. Duan, H. Xie, and H. Jiang, *Appl. Opt.* **52**(9), 1928 (2013).
- ¹⁷X. Zhang, H. F. Zhang, and S. Jiao, *J. Biomed. Opt.* **17**(3), 030502 (2012).

- ¹⁸M. Liu, Z. Chen, B. Zabihian, C. Sinz, E. Zhang, P. C. Beard, L. Ginner, E. Hoover, M. P. Minneman, R. A. Leitgeb *et al.*, *Biomed. Opt. Express* **7**(9), 3390 (2016).
- ¹⁹M. Tsai, H. Lee, C. Lee, C. Yu, H. Chen, C. Chiang, C. Chang, Y. Wang, and C. C. Yang, *Opt. Express* **16**(20), 15847 (2008).
- ²⁰W. Qi, T. Jin, J. Rong, H. Jiang, and L. Xi, *J. Biophotonics* **10**(12), 1580 (2017).
- ²¹T. Jin, H. Guo, H. Jiang, B. Ke, and L. Xi, *Opt. Lett.* **42**(21), 4434 (2017).
- ²²T. Jin, H. Guo, L. Yao, H. Xie, H. Jiang, and L. Xi, *J. Biophotonics*, e201700250 (2017).
- ²³H. Inoue, M. Kage, H. Ikeda, C. Sato, H. Sato, H. Minami, E. Santi, B. Hayee, and N. Eleftheriadis, *Ann. Gastroenterol.* **28**, 41–48 (2015).